A thermodynamic transient cross-bridge model for prediction of contractility and remodelling of the ventricle

Eoin McEvoy[1], William Wijns[2], Patrick McGarry[1*]

[1]Biomedical Engineering, National University of Ireland Galway
[2]The Lambe Institute for Translational Medicine, University Hospital Galway
[*]e-mail: patrick.mcgarry@nuigalway.ie

Abstract:

Cardiac hypertrophy is an adaption of the heart to a change in cardiovascular loading conditions. The current understanding is that progression may be stress or strain driven, but the multi-scale nature of the cellular remodelling processes have yet to be uncovered. In this study, we develop a model of the contractile left ventricle, with the active cell tension described by a thermodynamically motivated cross-bridge cycling model. Simulation of the transient recruitment of myosin results in correct patterns of ventricular pressure predicted over a cardiac cycle. We investigate how changes in tissue loading and associated deviations in transient force generation can drive restructuring of cellular myofibrils in the heart wall. Our thermodynamic framework predicts in-series sarcomere addition (eccentric remodelling) in response to volume overload, and sarcomere addition in parallel (concentric remodelling) in response to valve and signalling disfunction. This framework provides a significant advance in the current understanding of the fundamental sub-sarcomere level biomechanisms underlying cardiac remodelling. Simulations reveal that pathological tissue loading conditions can significantly alter actin-myosin cross-bridge cycling over the course of the cardiac cycle. The resultant variation in sarcomere stress pushes an imbalance between the internal free energy of the myofibril and that of unbound contractile proteins, initiating remodelling. The link between cross-bridge thermodynamics and myofibril remodelling proposed in this study may significantly advance current understanding of cardiac disease onset.

Keywords: Cardiac hypertrophy, cross-bridge cycling, finite element, myofibril remodelling

1. Introduction

Heart failure (the inability to pump sufficient blood to the body) often results from cardiac hypertrophy. This is a medical condition whereby the cardiomyocytes in the tissue wall remodel in response to an alteration in the mechanical environment (Carabello 2002; Grossman et al. 1975). Hypertrophy is typically categorised as concentric or eccentric. With eccentric hypertrophy the ventricle becomes thinner and longer, often onset by an increased diastolic blood volume (Figure 1 (right)) which may result from valve regurgitation (Carabello 1996; Lorell and Carabello, 2000). Cardiomyocytes undergo longitudinal cell growth and addition of sarcomeres in-series (Yoshida et al. 2010; Costabal et al. 2019). The contractility of this thin ventricle wall is dramatically reduced, and, consequently, the volume of blood ejected during systole is reduced, despite the fact that the enlarged ventricle can store an increased volume. In contrast, with concentric hypertrophy the tissue becomes thicker, often related to valve stenosis or aortic stiffening (Cho *et al.* 2015; Kupari *et al.* 2005; Carabello 2013). The number of parallel myofibrils in the cardiomyocytes increases, and the cells themselves also swell in size (Sawada and Kawamura 1991; Russell *et al.* 2010; Chien *et al.* 1993). Consequently, the ventricular chamber volume is reduced, leading to an insufficient volume of blood available for pumping during systole (Figure 1 (left)). With the onset of hypertrophy, there is reported to be prolonged calcium transients (Balke and Shorofsky, 1998; Bentivegna et al., 1991), possibly due to changes in the calcium re-uptake rate of the sarcoplasmic reticulum. Additionally, it is reported that pressure overload leads to increased synthesis of contractile proteins such as myosin heavy chain (Carabello, 2002; Cooper, 1997; Imamura et al., 1994).

Significant advances have been made in the field of cardiac biomechanics over the past 20 years, from a detailed imaging of the tissue myofibre micro-structure (LeGrice et al., 1995), to development of finite element models of anatomically accurate patient specific heart geometries (Wang et al., 2013). However, current finite element approaches typically use phenomenological formulations to represent tissue contractility (Pezzuto *et al.* 2014; Baillargeon *et al.* 2014). More detailed phenomenological models have also been developed based on experimentation that uncovered “fading memory” type behaviour in cardiomyocytes (Bergel and Hunter 1979; Hunter *et al.* 1998). In this paper we develop a model of the contractile left ventricle, with active cell tension and myofibril remodelling described by a thermodynamically motivated dynamic cross-bridge model. Simulations uncover a mechanism by which changes to the mechanical environment result in altered actin-myosin cross-bridge cycling, in turn driving remodelling of myofibrils in the heart wall. Mechanisms are uncovered for myofibrillar remodelling associated with eccentric and concentric hypertrophy due to increased diastolic volume and valve stenosis, respectively. The link between cross-bridge thermodynamics and myofibril remodelling proposed in this study can potentially significantly advance current understanding of cardiac disease onset.

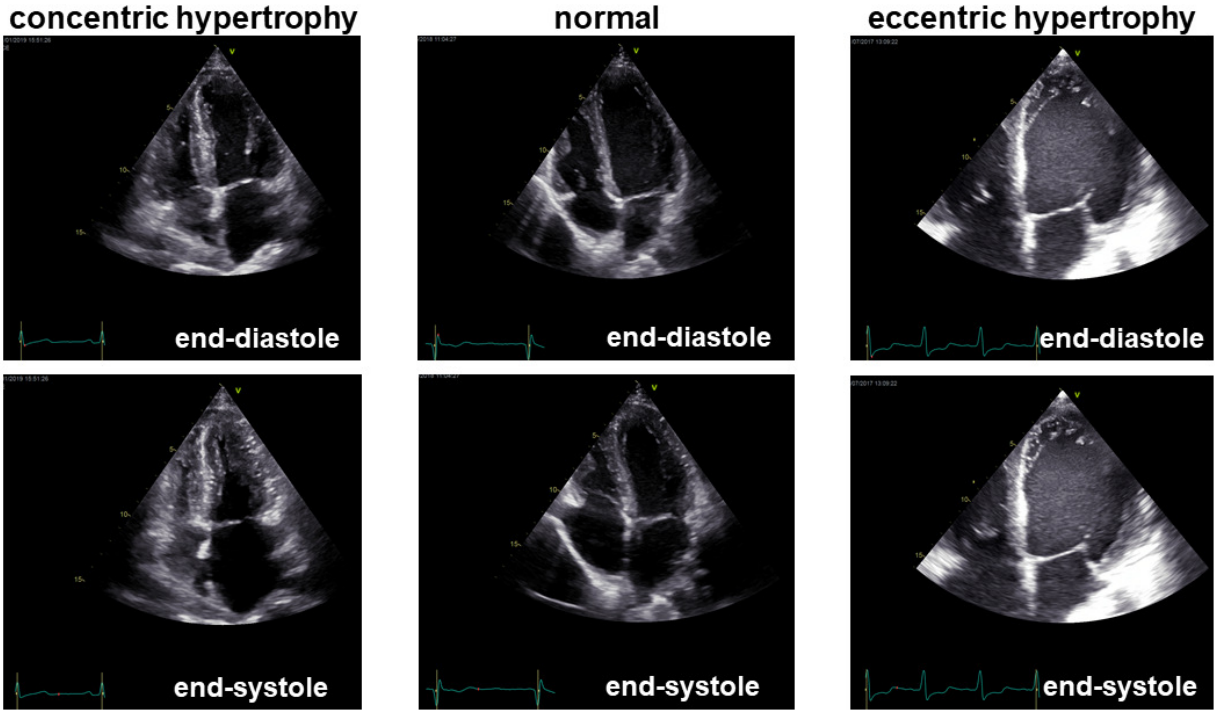

Figure 1: Echocardiography (4 chamber view) shows advanced structural changes at end-diastole and end-systole with concentric (left panels) or eccentric (right panels) hypertrophy. The left ventricle is shown in the upper right part of each image, with the apex on top and the left atrium at the bottom right. Compared to normal (central panels), concentric hypertrophy results in left ventricular wall thickening and cavity squeezing in systole. At the opposite, eccentric hypertrophy results in wall thinning and cavity dilatation. Courtesy of J.J. Bax and V. Delgado, Univ. of Leiden Medical Center.

2. Computational framework

2.1. Passive component of the myocardium model.

In addition to the high density of contractile cells in the ventricle wall, the myocardium contains a complex extracellular matrix (ECM) that supports the cells, and contributes significantly to the passive material behaviour. The tissue has a laminar architecture (Legrice et al., 1997), composed primarily of cardiomyocytes that bind together to form myofibre structures. Parallel arrangements of myofibres are bound by endomysial collagen which, along with other collagenous components and elastin, form individual myolaminae (sheets). These sheets vary in orientation throughout the ventricle wall. With this structure it is possible to define a local right-hand orthogonal set of axes to define the myofibre (*f*) direction, the cross-fibre or sheet (*s*) direction, and the normal (*n*) direction to this plane. The anisotropic biaxial and isochoric shear behaviour of the tissue has been well characterized (Dokos *et al.* 2002; Sommer *et al.* 2015), and is described by the Holzapfel and Ogden (2009) model, given as

$$\boldsymbol{\sigma}_{aniso} = \sum_{m=f,s} 2a_m(I_{4m}- 1)\exp[b_m(I_{4m}- 1)^2]\mathbf{a}_m\otimes\mathbf{a}_m + a_{fs}\, I_{8fs}\exp(b_{fs}{I_{8fs}}^2)(\mathbf{a}_f\otimes\mathbf{a}_s + \mathbf{a}_s\otimes\mathbf{a}_f), \quad (1)$$

where the first term on the right-hand side represents the mechanical contribution in the myofibre (*f*) and sheet (*s*) directions, and the second is an orthotropic term accounting for the shear contribution in the *f-s* plane. We implicitly consider that the stress in the myofiber direction is associated with deformation of both ECM and passive cell constituents (e.g. titin (Bartoo et al., 1997)). I_{4f}, I_{4s}, and I_{8fs} are anisotropic invariants defined as $I_{4f} = \mathbf{a}_{0f}.(\mathbf{C}\,\mathbf{a}_{0f})$, $I_{4s} = \mathbf{a}_{0s}.(\mathbf{C}\,\mathbf{a}_{0s})$, and $I_{8fs} = \mathbf{a}_{0f}.(\mathbf{C}\,\mathbf{a}_{0s})$. Full anisotropic invariants (e.g. I_{4f}) should be used in a compressible framework, as opposed to isochoric anisotropic invariants (e.g. $\bar{I}_{4f}$) (Nolan et al., 2014). The material tensor $\mathbf{C} = \mathbf{F}^{\mathrm{T}}\mathbf{F}$ is the right Cauchy-Green tensor, while $\mathbf{a}_{0m}$ $(m = f, s)$ is a unit vector indicating the myofibre or sheet orientations, and $\mathbf{a}_m$ is the same vector in the deformed configuration given by $\mathbf{a}_m = \mathbf{F}\,\mathbf{a}_{0m}$. The operator $\otimes$ is the dyadic product of vectors resulting in a second-order structure tensor. a_m and b_m $(m = f, s, fs)$ are anisotropic material parameters for each contribution.

A recent study by McEvoy *et al.* (2018) demonstrates that the myocardium is compressible, and the isotropic component of its mechanical behaviour is accurately described by a reduced polynomial Yeoh isotropic hyperelastic model (Yeoh, 1993). The Cauchy stress tensor for the isotropic compressible component of the myocardium is given as

$$\boldsymbol{\sigma}_{iso} = \sum_{i=1}^{3} \kappa_i\, i(J-1)^{2i-1}\mathbf{I} + \sum_{i=1}^{3} \mu_i\, i(\bar{I}_1 - 3)^{i-1}\left(\bar{\mathbf{B}} - \frac{1}{3}\bar{I}_1\mathbf{I}\right), \quad (2)$$

where the first term on the right-hand side represents the hydrostatic stress contribution due to volumetric deformation, and the second term represents the deviatoric stress contribution due to isochoric deformation. The positive scalar J is the determinant of the deformation gradient $\mathbf{F}$, $\mathbf{B} = \mathbf{F}\mathbf{F}^{\mathrm{T}}$ is the left Cauchy-Green tensor, with $\overline{\mathbf{B}} = J^{-\frac{2}{3}}\mathbf{B}$, and $\mathbf{I}$ is the identity tensor. The first invariant I_1 is the trace of $\mathbf{B}$, with $\overline{I_1} = J^{-\frac{2}{3}} I_1$, and κ_i, μ_i are volumetric and isotropic isochoric material parameters, respectively. The total passive Cauchy stress $\boldsymbol{\sigma}^{pas}$ follows as:

$$\boldsymbol{\sigma}^{pas} = \boldsymbol{\sigma}_{iso} + \boldsymbol{\sigma}_{aniso}. \tag{3}$$

2.2. Thermodynamic cross-bridge contractile model. Myofibrils in cardiomyocytes are comprised of individual sarcomere structures that actively generate tension via cross-bridge cycling. Previously we have proposed a model to describe the fundamental thermodynamics of actin-myosin interactions (McEvoy et al., 2019), that we extend here to consider cardiac specific interactions. We consider a 2-state model to account for the number of attached myosin heads (motivated by Huxley (1957)) at a given time. Within a sarcomere, there are a number of myosin heads m_{tot} available for attachment and subsequent cycling, with the rate of myosin binding given by:

$$\frac{d\hat{m}_a}{dt} = -k_d\hat{m}_a + k_a\hat{m}_d, \tag{4}$$

where $\hat{m}_a = m_a/m_0$ is the (normalised) number of attached myosin heads, where m_0 is the total number of myosin heads in the sarcomere, and $\hat{m}_d = m_d/m_0$ is the (normalised) number of unattached heads ($\hat{m}_d = \hat{m}_{tot} - \hat{m}_a$) The rate coefficients k_d and k_a are derived from the chemical potentials of the attached and unattached myosin heads under conditions of thermodynamic equilibrium, such that:

$$k_a = k_d \exp\left(\frac{\Delta\mu_{cb} - \phi_m + F\Delta_m}{k_B T}\right), \tag{5}$$

where $\Delta\mu_{cb} = \mu_a - \mu_d$ is the enthalpy difference between the attached and unattached myosin heads, k_B is the Boltzmann constant, and T is the absolute temperature. $F\Delta_{\mathrm{m}}$ is the work term, with $F = \delta\phi_m/\delta\Delta_{\mathrm{m}}$. The strain energy in the myosin tail is given by

$$\phi_m = \frac{1}{2}\kappa_m\Delta_m^2, \tag{6}$$

where κ_m is the tail stiffness (pN/nm), and Δ_m is the strain imposed on the tail. Myosin binding is significantly reduced during ventricular filling (diastole) due to low calcium signalling (Bootman and Bultynck, 2019; Frampton et al., 1991). Therefore we assume the influence of sarcomere lengthening on myosin tail strain need not be considered in this framework (for further details the reader is referred to McEvoy et al., 2019). Therefore, the strain imposed on the myosin tail only depends on isometric and shortening conditions, i.e.

$$\Delta_m = l_s + \Delta_m^s, \tag{7}$$

where l_s is strain induced in the myosin tail due to a tension generating stroke (caused by a change in configuration of the myosin head), and Δ_m^s is the offset in this strain caused by shortening of the sarcomere, given by

$$\Delta_m^s = \frac{L_{sarc}}{2}\,\dot{\tilde{\varepsilon}}_f\,t_s, \tag{8}$$

where $L_{sarc}/2$ is the length of a half sarcomere, $\dot{\tilde{\varepsilon}}_f$ is the sarcomere strain rate, and t_s is the period of time the myosin head remains attached during a cycle. Clearly, at isometric conditions ($\dot{\tilde{\varepsilon}}_f = 0$) Δ_m depends only on the stroke distance. The total number of myosin heads available for binding m_{tot} depends on the overlap s between the actin and myosin filaments, with the availability being a maximum at the optimum overlap s_0. A functional form for the overlap is given by a Cauchy-type distribution:

$$\hat{s} = \frac{1}{\varepsilon_s\pi\left(1 + \left(\frac{\tilde{\varepsilon}_f - \tilde{\varepsilon}_{ss}}{\varepsilon_s}\right)^2\right)s_0}, \tag{9}$$

where $\tilde{\varepsilon}_f$ is the internal nominal strain of a sarcomere, $\tilde{\varepsilon}_{ss}$ is the sarcomere strain at an optimal overlap, and ε_s is a distribution parameter. The distribution is normalized by $s_0 = 1/(\pi\,\varepsilon_s)$, which corresponds to an optimal overlap at $\tilde{\varepsilon}_f = \tilde{\varepsilon}_{ss}$. Additionally, myosin attachment in the myofibril is inhibited by a troponin-tropomyosin complex which blocks the actin binding site. An action potential in the ventricle wall triggers release of calcium, which subsequently binds to troponin and unblocks the actin binding site. Calcium transients is phenomenologically described by the approximate representation of intracellular Ca^{2+} twitch proposed by Hunter *et al.* (1998), given by:

$$\hat{Ca}_i = \left(Ca_0 + (Ca_{max} - Ca_0)\frac{t}{\tau_{Ca}}e^{1-\frac{t}{\tau_{Ca}}}\right)/Ca_{max}, \tag{10}$$

where t is the time since the most recent signal is initiated (following blood filling), Ca_0 is the resting calcium concentration, and Ca_{max} is the maximum concentration at time $t = \tau_{Ca}$. The availability of myosin heads depends both on the calcium transients and the overlap of the actin and myosin filaments. The total number of available myosin heads m_{tot} follows as

$$m_{tot} = \hat{s}\,\hat{Ca}_i\,m_0\,, \tag{11}$$

where m_0 is the total number of myosin heads in the sarcomere. The sarcomere stress is computed as a function of the tension in the myosin and the total number of active heads:

$$\sigma_s = \hat{m}_a\kappa_m\Delta_m\rho_{ma}, \tag{12}$$

where $\rho_{ma} = m_0/A_{sarc}$ is the area density of myosin heads in the sarcomere, and A_{sarc} is the sarcomere cross-sectional area.

2.3. Myofibril remodelling. Within cardiomyocytes in the ventricle wall, there is a high density of contractile myofibrils composed of actin-myosin sarcomeres. These myofibrils actively generate tension via cross-bridge cycling, as described in Section 2.2. This thermodynamically motivated cross-bridge cycling model is used in conjunction with a thermodynamically consistent framework for sarcomere remodelling (Vigliotti et al., 2015) to uncover the relationship between actin-myosin tension generation and structural remodelling at the myofibril scale. Here we summarise key equations of the sarcomere remodelling framework.

Consider an existing myofibril comprised of a reference number of sarcomeres n^R in-series (each of uniform length L_{sarc}). Should a nominal material strain ε_f be applied to the cell (and directly translated to the myofibrils), it will cause a change in the overlap s between the actin and myosin filaments of the individual sarcomeres. A remodelling process is initiated to achieve an optimal actin-myosin overlap (i.e. equation 9; $s = s_0$), which, for example, will result in $n = n^R(1 + \tilde{\varepsilon}_{ss})$ sarcomeres along the myofibril's length at steady state, provided contractile proteins are available. Following remodelling, the internal strain within a sarcomere $\tilde{\varepsilon}_f$ will differ from an applied material strain, such that

$$\tilde{\varepsilon}_f = \frac{1 + \varepsilon_f}{\hat{n}} - 1, \tag{13}$$

where $\hat{n} = n/n^R$. The case of a sarcomere strain $\tilde{\varepsilon}_f > \tilde{\varepsilon}_{ss}$ would result in the addition of sarcomeres in-series, with sarcomeres removed at $\tilde{\varepsilon}_f < \tilde{\varepsilon}_{ss}$. The kinetic law for remodelling is given as

$$\dot{\hat{n}} = \begin{cases} -\frac{1}{\hat{n}}\left(\frac{\widehat{N}_u}{\hat{\eta}}\right)^2 \left[\psi(\tilde{\varepsilon}_f) - \frac{\delta\psi}{\delta\tilde{\varepsilon}_f}(1 + \tilde{\varepsilon}_f)\right]\frac{\alpha_n}{\mu_{b0}}, & if\ \frac{\delta\Psi}{\delta n} \leq 0 \\ -\frac{\hat{n}}{4}\left[\psi(\tilde{\varepsilon}_f) - \frac{\delta\psi}{\delta\tilde{\varepsilon}_f}(1 + \tilde{\varepsilon}_f)\right]\frac{\alpha_n}{\mu_{b0}}, & otherwise, \end{cases} \tag{14}$$

where $\widehat{N}_u$ is the (normalized) number of available contractile proteins, $\hat{\eta}$ is the concentration of myofibrils, and α_n is a rate constant. The internal energy of n^R sarcomeres ψ increases as the internal strain $\tilde{\varepsilon}_f$ changes, with a functional form given by

$$\psi = \mu_{b0} + \beta\mu_{b0}\left|\tilde{\varepsilon}_f\right|^p, \tag{15}$$

where μ_{b0} is the internal energy of n^R sarcomeres in their reference state, and β and p are non-dimensional constants that govern the sarcomere strain at an optimal overlap $\tilde{\varepsilon}_{ss}$, such that

$$(p-1)\tilde{\varepsilon}_{ss}^p + p\tilde{\varepsilon}_{ss}^{p-1} - \frac{1}{\beta} = 0\,. \tag{16}$$

The rate of change of the internal energy follows as

$$\frac{\delta\Psi}{\delta n}\dot{n} = \dot{\hat{n}}\left[\psi(\tilde{\varepsilon}_f) - \frac{\delta\psi}{\delta\tilde{\varepsilon}_f}(1 + \tilde{\varepsilon}_f)\right]. \tag{17}$$

Formation and dissociation of myofibrils is governed by thermodynamic equilibrium of proteins available for binding (unbound), and those already bound in sarcomeres. The standard enthalpy μ_b of n^R sarcomeres within a myofibril is written as

$$\mu_b = \psi - \sigma_s\left[1 + \tilde{\varepsilon}_f\right]\Omega\,, \tag{18}$$

where Ω is the volume of n^R sarcomeres in a myofibril, and σ_s is the sarcomere stress (equation 12). Unbound proteins are affected by an activation signal level, and tend to transform into their bound states more readily when such signalling is increased. The standard enthalpy μ_u of unbound proteins follows as

$$\mu_u = \mu_{u0} + \Delta\mu_{u0}\hat{C}_f, \tag{19}$$

where μ_{u0} is the standard enthalpy of the unbound proteins in the absence of a formation signal $\hat{C}_f$ and $\Delta\mu_{u0}$ is the increase in the enthalpy of the unbound molecules at full activation ($\hat{C}_f = 1$). Fibre formation may be further initiated by a biochemical or mechanical perturbation that triggers a signalling cascade within the cell e.g. titin-associated pathways (Knöll et al., 2002), but as such pathways are not fully understood (Krüger and Kötter, 2016) we consider a constant signal in the current analysis (i.e. $\hat{C}_f = 1$). The rate of myofibril formation/ dissociation follows as

$$\dot{\hat{\eta}} = \frac{\widehat{N}_u}{\hat{n}}\omega_n \exp\left[-\hat{n}\frac{\mu_{ab} - \mu_u}{k_B T}\right] - \hat{\eta}\,\omega_n\, exp\left[-\hat{n}\frac{\mu_{ab} - \mu_b}{k_B T}\right] \tag{20}$$

where ω_n is the collision frequency of the unbound molecules, and μ_{ab} is an activation barrier. The (normalized) number of unbound proteins may be calculated as

$$\widehat{N}_u = \widehat{N}_t - \hat{\eta}\hat{n}, \tag{21}$$

where $\hat{\eta}\hat{n}$ determines the (normalized) number of bound proteins, and $\widehat{N}_t$ is the total (normalized) number of contractile proteins. Following Vigliotti *et al.* (2015), in this study we assume a constant turnover of contractile proteins, i.e. synthesis rate = degradation rate (however, the effect of increased protein synthesis (associated with aortic stenosis and concentric hypertrophy) is also investigated in Section 4.2.4). As the cardiomyocytes are oriented in the previously defined myofibre (*f*) direction, the Cauchy stress due to fibre contractility is given by

$$\boldsymbol{\sigma}^{act} = \hat{\eta}\,\sigma_s f_0\,\mathbf{a}_f \otimes \mathbf{a}_f, \tag{22}$$

where f_0 is the volume fraction of cardiomyocytes in the heart wall. Finally, the total Cauchy stress may be calculated as a function of the active and passive contributions, such that

$$\boldsymbol{\sigma}^{tot} = \boldsymbol{\sigma}^{pas} + \boldsymbol{\sigma}^{act}. \tag{23}$$

2.4. Finite element implementation. In this section, development of an idealised 3D finite element model of the left ventricle is presented. A solid model of the generic heart is created by means of a truncated ellipsoid (Figure 2A), motivated by the passive ventricle models of Göktepe et al. (2011) and Rausch et al. (2011), and discretized with 26524 hexahedral elements. All finite element simulations are performed using Abaqus/Explicit (v2017, DS Simulia, RI, USA), and constitutive equations (equations 1-23) are implemented via user-defined material subroutines (VUMATs). The basal surface is constrained in the global axial direction. As mentioned previously, a local right-hand orthogonal set of axes may be established, denoting the myofibre (f), sheet (s), and normal (n) directions. The sheet direction is assumed to orient normal to the endocardial and epicardial ventricle walls, while the orientation of the myofibres varies transmurally by an angle θ. This angle changes from approximately 70° at the endocardium to -70° at the epicardium, with respect to the circumferential direction and rotated about the sheet axis (Figure 2B). The wall thickness is discretized into nine regions, with θ assumed to be uniform within each region, as are the myofibril concentration $\hat{\eta}$ and the number of in-series sarcomeres $\hat{n}$. Remodelling of $\hat{\eta}$ and $\hat{n}$ is restricted in the finite element simulations (i.e. $\dot{\hat{n}} = \dot{\hat{\eta}} = 0$). For numerical efficiency remodelling is simulated within a submodelling framework (Section 3).

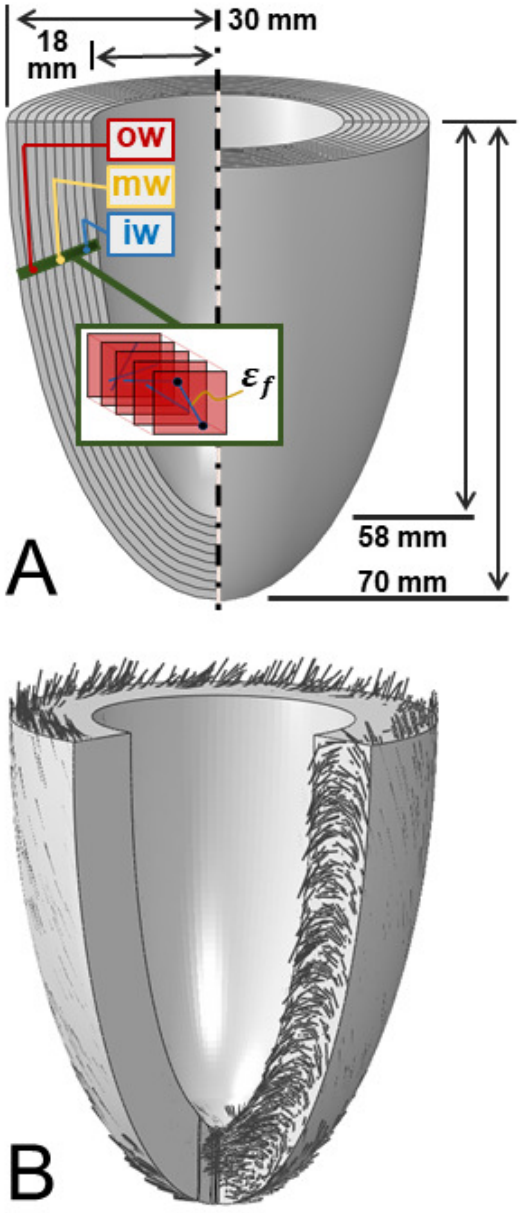

Figure 2: A) Geometry of an idealised left ventricle model with highlighted zones for inner-wall (iw), mid-wall (mw) and outer-wall (ow); b) transmural variation of myofibre (f) orientation.

2.5. Model Parameters. Material constants for the passive anisotropic hyperelastic model are fixed to those previously calibrated to experimental data from human tissue by McEvoy *et al.* (2018). The anisotropic constants are $a_f = 2.75\ kPa$, $b_f = 32.1$, $a_s = 1.06\ kPa$, $b_s = 30.1$, $a_{fs} = 0.175\ kPa$, and $b_{fs} = 5.02$. The isotropic constants for the compressible formulation are $\mu_1 = 0.98\ kPa$, $\kappa_1 = 7.31\ kPa$, $\mu_2 = -0.212\ kPa$, $\kappa_2 = 5.12\ kPa$, $\mu_3 = 22.68\ kPa$, and $\kappa_3 = 2.49e6\ kPa$. All simulations are reported for cells at a normal body temperature $T = 310\ K$. For the cross-bridge cycling model, the myosin head stroke distance $l_s = 6.5\ nm$, the myosin tail stiffness $\kappa_m = 1.75\ pN\ nm^{-1}$ are based on the range of values reported previously (Huxley 1957; Smith and Geeves 1995; Offer and Ranatunga 2013). The length of a cardiomyocyte half sarcomere L_{sarc} is taken to be $900\ nm$ (Nguyen et al., 2017). The volume fraction of cardiomyocytes in the heart wall f_0 is 0.75 (Tang et al., 2009; Zhou and Pu, 2016). The area density of myosin heads within a sarcomere $\rho_{ma} = 0.056\ /nm^2$ lies within measured ranges (Harris et al., 2011; Millman, 1998). The remaining cross-bridge cycling model parameters are calibrated such that a myofibril volume fraction of ~50% and a physiological ventricular pressure are predicted for boundary conditions that simulate a healthy cardiac performance, as described in Sections 3.1 and 4.1; namely $\Delta\mu_{cb} = 9k_BT$; $t_s = 6\ ms$; $k_d = 12\ s^{-1}$, $\mu_{u0} = \Delta\mu_{u0} = 4.49k_BT$ (see influence on sarcomere remodelling in SI Figure S1). The parameters for the calcium transients model are fixed at those reported by Hunter *et al.* (1998), such that the maximum calcium concentration Ca_{max}=1μM, the resting level value $Ca_0 = 0.01\mu M$, and the time constant $\tau_{Ca} = 60\ ms$. The parameters for the myofibril remodelling framework are confined to ranges reported by Vigliotti *et al.* (2015); McEvoy *et al.* (2019), with $\Omega = 10^{-7.1}\mu m^3$, $\beta = 1.2$, $p = 2$, $\varepsilon_s = 0.225$, and $\widehat{N}_t = 1$. The enthalpies of the contractile proteins are, $\mu_{b0} = 9k_BT$, and $\mu_{ab} = 20k_BT$, and the remodelling rates $\omega_n = 100\ Hz$ and $\alpha_n = 25\ mHz$.

3. Simulation procedure

3.1. Physiological Conditions. Volumetric boundary conditions are applied to the ventricle wall via nodal displacements within a VDISP subroutine (Figure 3A). The

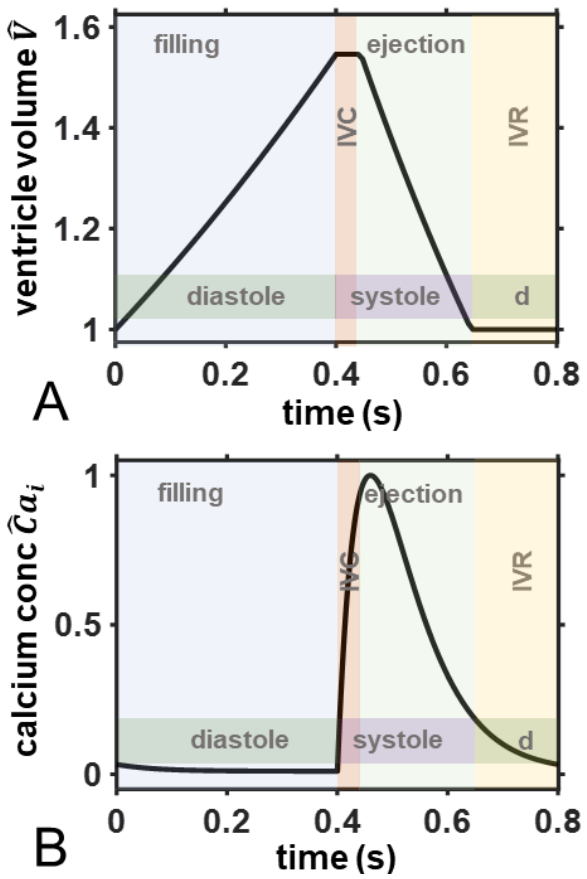

Figure 3: Applied boundary conditions for simulation of healthy cardiac cycle: A) volume ($\hat{V} = V/V_0$) of the ventricular chamber; b) calcium concentration $\hat{C}a_i$ to unblock actin binding sites. Durations are highlighted for blood filling, isovolumetric contraction (IVC), blood ejection, and isovolumetric relaxation (IVR).

volume of the ventricular chamber increases during filling ($t \leq 0.4s$) and remains fixed during isovolumetric contraction (IVC) for $t_{hold} = .045s$. At the beginning of systole, a uniform calcium twitch is initiated (as shown in Figure 3B). The ejection phase is simulated by a reduction in the ventricular volume over $0.2s$; a linear decrease is assumed. In an initial simulation, a pressure of 10 mmHg is applied to the inner ventricle surface (pressure associated with ventricular filling), and the nodal displacements are stored. An iterative multi-scale procedure is developed to determine the evolution of the myofibril concentration $\hat{\eta}$ and the number of in-series sarcomeres $\hat{n}$ (within cells) throughout the heart wall, resulting in the prediction of a heterogeneous steady state distribution following the simulation of several cardiac cycles. The active contractility of this heterogeneous distribution of myofibrils in the heart wall directly results in an increase in ventricle pressure during IVC, in addition to a temporally varying pressure during systole. In order to compute the heterogeneous distribution of $\hat{\eta}$ and $\hat{n}$ the following steps are implemented, as illustrated in Figure 4.

The submodel numerical framework (equations 4-21) is solved via a Runge–Kutta iterative method in Matlab, with the loading condition governed by ε_f. As described in Figure 4, the following steps then take place:

(i) Spatially uniform initial conditions of $\hat{\eta} = 0.4$ and $\hat{n}$=0.7 are assumed throughout the heart wall. The cardiac cycle is simulated in the full ventricle model through application of volume boundary conditions and calcium-initiated contractility, as shown in Figure 3. The temporally varying axial material strain in the myofibre direction throughout a cardiac cycle, $\varepsilon_f(t)$, is computed at each integration point in the mesh.

(ii) For each integration point a submodel is used to determine the evolution of $\hat{\eta}$ and $\hat{n}$ (using a Runge–Kutta iterative method in Matlab) in response to the myofibre axial strain history $\varepsilon_f(t)$. A large number of cardiac cycles (>500) are simulated until steady state values of $\hat{\eta}$ and $\hat{n}$ are attained for the integration point in question.

(iii) The steady state values for $\hat{\eta}$ and $\hat{n}$ determined by the sub-model for each integration point are then input to the global finite element model of the ventricle. This provides a spatially heterogeneous distribution of $\hat{\eta}$ and $\hat{n}$.

(iv) The cardiac cycle is simulated again in the full ventricle with the updated heterogeneous distribution of $\hat{\eta}$ and $\hat{n}$. Again, the strain histories throughout the cardiac cycle at each integration point, $\varepsilon_f(t)$, are recorded and used as input to the sub-model. The predicted temporally varying ventricle pressure is also recorded.

(v) Steps (i)-(iv) are repeated until $\hat{\eta}$ and $\hat{n}$ change by <1% between iterations at each integration point.

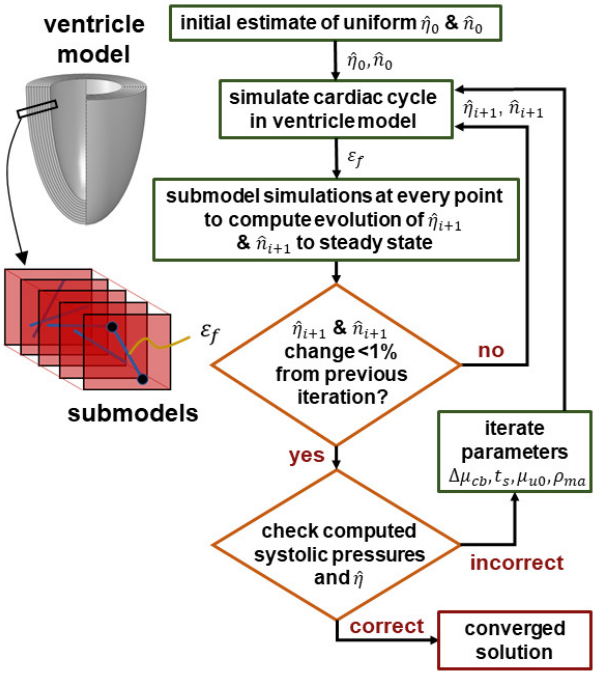

Figure 4: Flowchart of model solution scheme.

(vi) Following computation of a converged heterogeneous distribution of $\hat{\eta}$ and $\hat{n}$, the following checks are performed for the computed ventricular pressure:
(a) $75\ mmHg < P(end\ IVC) < 85\ mmHg$, and
(b)$115\ mmHg < P(peak\ systole) < 125\ mmHg$.
Additionally, it is checked that the computed range of $\hat{\eta}$ throughout the myocardium satisfies the following criterion (Sommer and Johnson 1979):
(c) $0.4 < \hat{\eta} < 0.6$.

(vii) If criteria (a-c) above are not satisfied, the procedure is repeated for new values of the parameters $\Delta\mu_{cb}$, t_s, μ_{u0}, and k_d.

3.2. Perturbations from healthy loading conditions (pathological loading). Cardiac hypertrophy is commonly assumed to onset due to a change in the mechanical environment of the myocardium. Following the calibration of healthy tissue in Section 3, a series of pathological loading conditions are applied to the ventricular model to approximate biomechanical conditions that have been clinically observed to result in eccentric and concentric hypertrophy. Eccentric hypertrophy is clinically reported to develop predominantly due to an increased diastolic ventricular blood volume. Such an increased ventricular blood volume can be associated with aortic or mitral regurgitation (Lorell and Carabello 2000; Gotzmann *et al.* 2012; Maurer 2006; Gaasch and Meyer 2008). We simulate such altered loading by increasing the maximum applied volume change by ~40% while keeping the stroke volume constant. Concentric hypertrophy is reported to develop due to a range of pathologies, including aortic stenosis (Carabello and Paulus 2009; Kupari *et al.* 2005) and hypertension (de Simone, 2004). In this study, we investigate the influence of a stenotic valve on hypertrophic remodelling. Specifically, we analyse the effect of a stiffened valve increasing the duration of IVC by ~30 ms. Progression of concentric hypertrophy has also been linked to prolonged calcium transients (Balke and Shorofsky, 1998; Bentivegna et al., 1991), and increased contractile protein synthesis (Carabello, 2002; Cooper, 1997; Imamura et al., 1994). Therefore, these pathologies are also examined by increasing the time constant in the calcium transients τ_{Ca} to 75 ms, and increasing the total number of contractile proteins $\widehat{N}_t$ by 10%, respectively. Initial values of $\hat{\eta}$ and $\hat{n}$ are determined from predicted distributions (Figures 5e and 5f) under physiological loading (Section 4.1). As per Section 3.1 the material strain ε_f (recorded under pathological loading) is reapplied to a submodel framework. The following conditions are examined:

(i) Increased diastolic ventricular volume (IV): Increase the peak diastolic blood volume to $\widehat{V}_{max} = 1.76$ during the cardiac cycle (Figure 6A);
(ii) Obstruction to ventricular outflow due to valve stenosis (VS): Increase the duration of IVC via $t_{hold} \rightarrow 75\ ms$ (stiffened aortic valve) (Figure 7A);
(iii) Prolonged calcium transients (PC): Increase duration of calcium transients via $\tau_{Ca} \rightarrow 75\ ms$ (Figure 8A).
(iv) Increased protein synthesis (IP): Increase the total number of contractile proteins via $\widehat{N}_t \rightarrow 1.1$ (Figure 9A).

We examine the influence of such conditions on remodelling of the number of in-series sarcomeres $\hat{n}$, remodelling of the parallel concentration of myofibrils $\hat{\eta}$, and the resulting pressure-volume loop. Subsequent events in hypertrophy, such as alterations in cell size, shape, and myocardium growth, are not considered in the current study, but will be addressed in future developments of this framework.

4. Results

4.1. Predictions for healthy state. Simulations for a normal heart under physiological conditions were performed for the analysis described in Section 3.1. As described in Section 3.1 a converged solution is attained for the concentration of myofibrils, $\hat{\eta}$, and the number of in-series sarcomeres, $\hat{n}$, throughout the ventricle wall. The predicted ventricle pressure-volume loop for the final calibrated model parameters ($\Delta\mu_{cb} = 9k_BT$, $t_s = 6\ ms$, $\mu_{u0} = 4.49\ k_BT$, and $k_d = 12\ s^{-1}$) is shown in Figure 5A. During blood filling in diastole ($0\ s \leq t < 0.4\ s$, the ventricle pressure increases to 10 mmHg. As the calcium concentration remains at Ca_0 during this time, the increase in the ventricle wall stress is due to deformation of the passive tissue constituents (via equations 1-3). At the beginning of IVC the calcium concentration (Figure 3B) increases rapidly, resulting in unblocking of the actin binding sites. This allows for attachment of myosin heads and cross-bridge cycling. The transient attachment of myosin heads $\widehat{m}_a$ as shown in Figure 5B is governed by equations (4-12). An active tension (generated through cross-bridge cycling of the attached myosin heads) transiently increases during IVC, resulting in an increase in the ventricle pressure to ~80 mmHg by the end of IVC (Figure 5A). During systole the ventricle volume and the calcium concentration reduces (Figure 3B). However, $\widehat{m}_a$ continues to increase during the early stages of diastole. This transient response is due to the thermodynamically motivated kinetic equation for myosin binding and unbinding (equations 4-5). The resultant increase in actively generated tension leads to an increase in ventricle pressure to a peak value of ~120 mmHg at time $t = 0.552\ s$ (Figure 5A). However, the rate at which the contractility increases is reduced following IVC due to shortening of the ventricle wall. Such shortening reduces the myosin attachment rate by lowering the strain energy ϕ_m of the myosin tail (via equations 6-8). In the latter stages of systole, the number of attached myosin heads, $\widehat{m}_a$, decreases due to the continually reducing signal (and further shortening of the ventricle wall). As a result the ventricle pressure is predicted to decrease to a value of 60 mmHg by the end of systole. Figure 5C shows the stress distribution in the ventricle at the point of peak systolic pressure ($t = 0.552\ s$). This stress includes a passive and active contribution, and is predicted to be highest at the inner and mid-section of the myocardium (60-70 kPa). At the mid-section, the fibre stretch is highest due to myofibre alignment in the circumferential direction (i.e. 0° rotation). Significant torqueing/twisting of the ventricle is computed

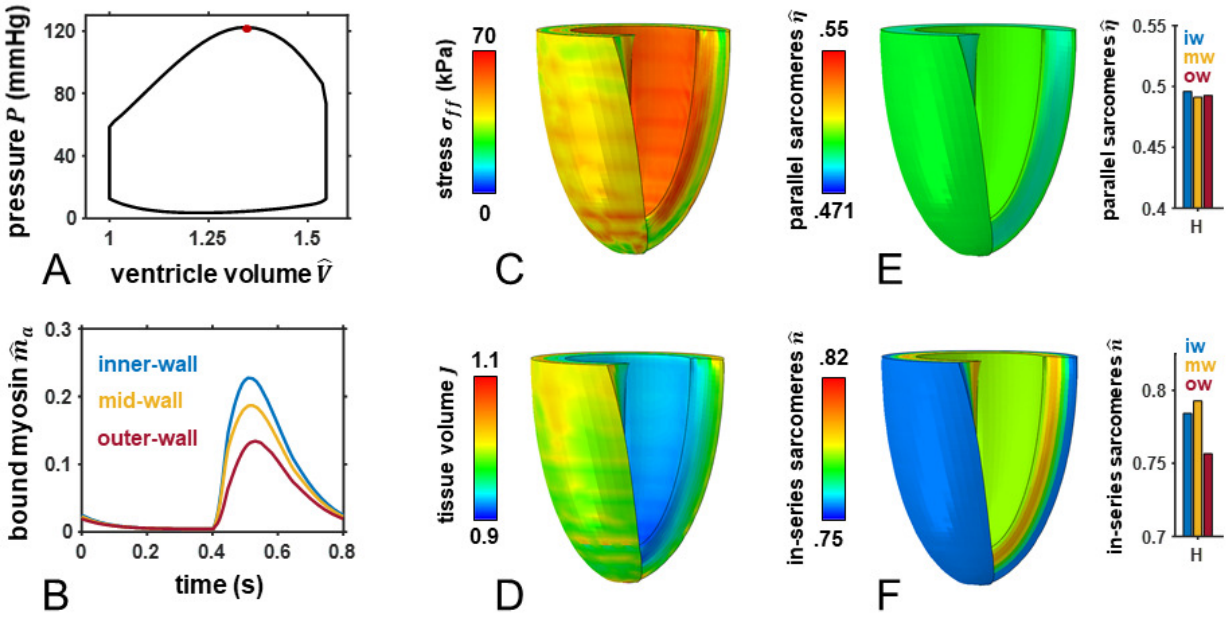

Figure 5: Physiological loading (H): Predicted A) ventricular pressure-volume loop and B) number of active myosin heads $\hat{m}_a$ over a single cardiac cycle; Contour plots are shown at peak systole ($t = 0.552$s, red circle in (A)) for C) the Cauchy stress in the myofibre (f) direction σ_{ff}, D) the material volume J, E) the concentration of myofibrils $\hat{\eta}$, and F) the number of in-series sarcomeres $\hat{n}$. Adjoining bar plots show local values in zones iw, mw, and ow.

over the course of the cardiac cycle due to the complex distribution of myofibres across the tissue wall. Such torqueing is physiological and has been reported clinically by Sengupta *et al.* (2008). As shown in Figure 5D, a slight decrease in the myocardium tissue volume is computed during systole due to the high levels of contractility generated by the myofibres. This tissue co mpaction is more pronounced at the inner wall ($8\% - 10\%$ local tissue volume reduction) compared to the outer wall (< 2% local tissue compaction). These predicted patterns of spatially heterogeneous tissue compaction during systole are supported by the in-vivo measurements of Ashikaga *et al.* (2008). The converged value s for myofibril concentration $\hat{\eta}$ and number of in-series sarcomeres $\hat{n}$ are shown in Figure 5E and Figure 5F, respectively. As there is very little change in the material strain circumferentially or axially (due to the axisymmetry and idealised geometry of the model), significant differences in $\hat{\eta}$ and $\hat{n}$ are only predicted transmurally. The predicted myofibril concentration $\hat{\eta}$ is predicted to vary from ~0.485 – 0.505 across the wall, in agreement with reported concentrations (Sommer and Johnson 1979; Linke *et al.* 1994). $\hat{n}$ is predicted to be highest at the inner- and mid-wall (iw and mw, respectively), as the material strain is highest in these regions. High myocardial strains are avoided at the outer wall due to high stress generated by circumferentially aligned myofibres at the mid-wall.

4.2. Predictions for pathological loading.

Increased diastolic ventricular volume (IV). Eccentric hypertrophy is reported to occur in the myocardium in response to an increase of the diastolic blood inflow to the ventricle (Figure 6A). As shown in Figure 6B, the increased ventricular volume is shown to result in an increased pressure during both diastole and systole. The increased volume during diastole (reflecting an increase in venous return) causes an increase in passive stretching of the heart wall, and consequently an increased passive stress in the wall. Furthermore, in response to this increased wall stretch, the number of in-series sarcomeres within cells in the heart wall is predicted to increase (Figure 6D) (i.e. $\hat{n}$ increases to ~0.82 at the myocardium mid-wall (mw)). Recall that our model suggests myofibrils remodel the number of in-series sarcomeres in order to reduce their free energy (by maximising active stress generated through cross-bridge cycling). The higher myocardial wall strain increases the internal sarcomere strain $\tilde{\varepsilon}_f$, and thus the difference between $\tilde{\varepsilon}_f$ and $\tilde{\varepsilon}_{ss}$ (optimal overlap strain). This reduces the actin-myosin overlap via equation 9 (Figure 6F (dotted lines)). A reduction in the overlap lowers the availability of myosin heads m_{tot} and therefore reduces the number of attached myosin heads (equation 11). This lowers the active contractility and thus increases the sarcomere free energy. The myofibril remodels such that additional sarcomeres $\hat{n}$ are added in-series (via equations 14-16), increasing the overlap of the actin and myosin filaments during the highly contractile regime (Figure 6F (solid line)). This in turn increases $\hat{m}_a$ (Figure 6E) and the active tension, and reduces the free energy of individual sarcomeres. Importantly, due to of the conservation of the number of contractile proteins (equation 21), the parallel concentration of myofibrils $\hat{\eta}$ is lowered (Figure 6C) relative to the healthy tissue (Figure 6E). This results in a reduction in the active myocardium stress during systole. The slight increase in peak systole pressure shown in Figure 6B occurs because this decrease in active stress is outweighed by the aforementioned increase in passive stress. In summary, simulations predict an increase in the number of in-series

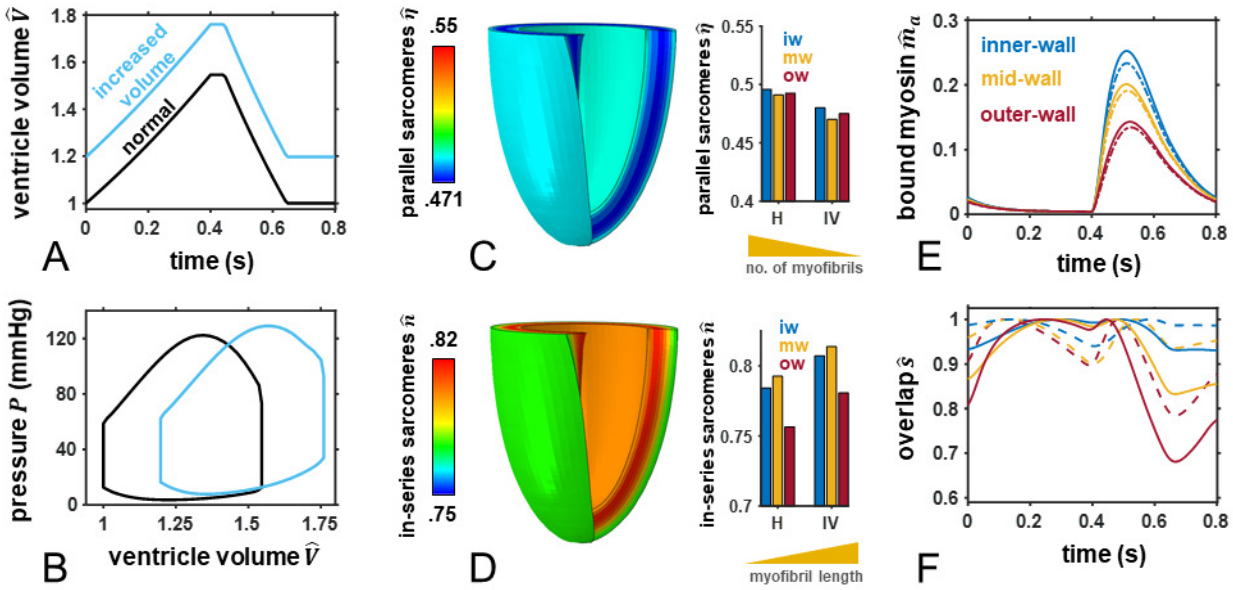

Figure 6: Increased diastolic ventricular volume (IV): A) Applied volume and B) predicted pressure-volume loop over a single cardiac cycle (black line shows the healthy state for reference); Contour plots are shown at peak systole ($t = 0.552s$) for C) the concentration of myofibrils $\hat{\eta}$ and D) the number of in-series sarcomeres $\hat{n}$. Adjoining bar plots show local values in zones iw, mw, and ow; For a single cardiac cycle the predicted E) number of attached myosin heads $\hat{m}_a$ (dotted line shows healthy state for reference) and F) overlap $\hat{s}$ of the actin and myosin filaments are shown for zones iw, mw, and ow (dotted lines show the overlap $\hat{s}$ prior to remodelling of $\hat{\eta}$ and $\hat{n}$). For IV analysis $\hat{V}_{max} = 1.76$.

sarcomeres within cardiomyocytes in the heart wall in response to an increased diastolic blood volume.

Valve stenosis (VS). Concentric hypertrophy is commonly observed clinically in response to an obstructed outflow, such as aortic valve stenosis (Kupari *et al.* 2005). This pathology is simulated by increasing the duration of IVC (t_{hold}) (Figure 7A), as described in Section 3.2. As shown in Figure 7B this r esults in an increase in ventricular pressure during IVC to ~145 mmHg, and also promotes an increase in myofibril concentration, $\hat{\eta}$, across the heart wall (Figure 7C). No change is predicted in the distribution of sarcomeres in-series $\hat{n}$ (Figure 7D) relative to the healthy state, as the overlap $\hat{s}$ is not altered significantly (Figure 7F) by these boundary conditions. The prolonged IVC duration ($+30\ ms$) maintains the myofibrils/ sarcomeres at isometric conditions for longer (i.e. equation 7: $\Delta_m^s = 0$). Such isometric conditions during a period of a strong calcium ($\hat{C}a_i$) concentration results in a significant increase in myosin attachment across the heart wall, as shown in Figure 7E, and an associated increase in the actively generated sarcomere tension. This promotes an increase in myofibril concentration, $\hat{\eta}$, via a reduction in the internal sarcomere free energy (equation 18). Furthermore, the increased sarcomere/cell stress contributes to increasing the ventricular pressure (Figure 7B). In summary, simulations predict an increase in parallel myofibril concentration in response to prolonged closure of the aortic valve, associated with stenosis.

Prolonged calcium transients (PC). Next, we investigate the influence of a prolonged calcium transients (Figure 8A) on myofibril remodelling, as described in Section 3.2. Simulations predict that such signalling results in an increase in peak systolic pressure (Figure 8B), an increase in $\hat{\eta}$ of ~5% across the wall (Figure 8C), and a reduction in $\hat{n}$ (Figure 8D). The longer signal duration allows for additional attachment of myosin heads (Figure 8E), resulting in a higher sarcomere stress. Therefore, a higher parallel concentration of myofibrils is predicted due to a reduction in the internal sarcomere free energy (equation 18), following a similar pathway as remodelling due to valve stenosis. The increased contractility (due to an extended signal duration) results in a lower wall stretch at the mid- and oute r-regions (not inside wall due to applied constraint), thereby modifying the actin myosin overlap $\hat{s}$ (Figure 8F) and promoting a reduction in $\hat{n}$ within these regions. In summary, simulations predict a significant increase in the parallel myofibril concentration in response to prolonged calcium transients.

Increased protein synthesis (IP). It has been suggested that the increased cardiomyocyte mechanical output leads to increased synthesis of contractile proteins (Carabello, 2002; Cooper, 1997; Imamura et al., 1994). We examine the influence of such increased synthesis on myofibril remodelling by increasing the concentration of contractile proteins, $\hat{N}_t$, by 10% (Figure 9A), as described in Section 3.2. Such an increase is shown to lead to higher ventricular pressure over the course of the cardiac cycle (Figure 9B), due predominantly to an increase in myofibril formation (Figure 9C). In contrast, the increased pr otein concentration does not significantly alter the in-series distribution of sarcomeres, $\hat{n}$, (Figure 9D) as no significant changes are computed in the sarcomere strains and the actin-myosin overlaps $\hat{s}$ (Figure 9F) compared to the healthy tissue. An

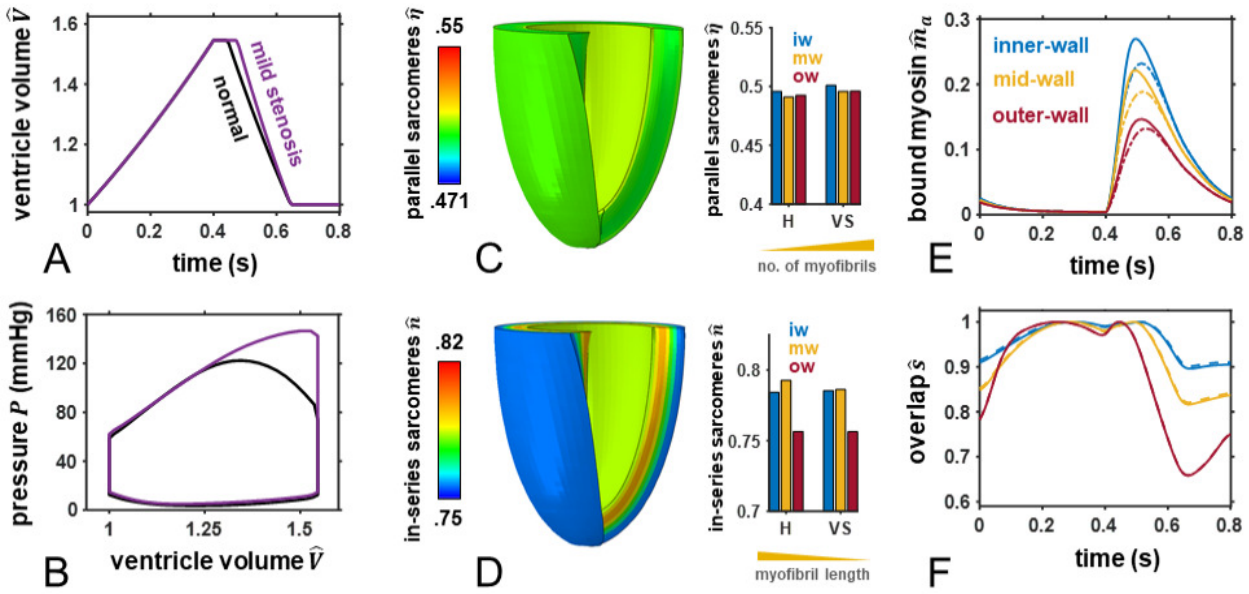

Figure 7: Valve stenosis (VS): A) Applied volume and B) predicted pressure-volume loop over a single cardiac cycle (black line shows the healthy state for reference); Contour plots are shown at peak systole ($t = 0.552s$) for C) the concentration of myofibrils $\hat{\eta}$ and D) the number of in-series sarcomeres $\hat{n}$. Adjoining bar plots show local values in zones iw, mw, and ow with reference to healthy state; For a single cardiac cycle the predicted E) number of attached myosin heads $\hat{m}_a$ (dotted line shows healthy state for reference) and F) overlap $\hat{s}$ of the actin and myosin filaments are shown for zones iw, mw, and ow (dotted lines show the overlap $\hat{s}$ prior to remodelling of $\hat{\eta}$ and $\hat{n}$). For VS analysis $t_{hold} = 75\ ms$.

increase in $\widehat{N}_t$ promotes additional formation of myofibrils by increasing the chemical potential of the unbound contractile proteins. In order to achieve chemical equilibrium between the proteins in a bound and unbound state, the concentration of myofibrils in parallel, $\hat{\eta}$, therefore increases (via $\widehat{N}_u$; equation 20). While the concentration of attached myosin heads per sarcomere remains unaffected by the increase in $\widehat{N}_t$ (Figure 9E), the increase in $\hat{\eta}$ results directly in an increase in actively generated contractile stress in the myocardium (equati on 21), which directly results in an increase in ventricle pressure. In summary, simulations predict a significant increase in the parallel myofibril concentration in response to increased contractile protein synthesis.

5. Concluding remarks

In this study we implement a thermodynamically motivated model for myofibrillar cross-bridge cycling and remodelling, coupled with a compressible anisotropic hyperelastic framework, to simulate the behaviour of the ventricular myocardium during the cardiac cycle. Homeostatic concentrations of myofibrils are first determined for a healthy heart under normal physiological loading conditions. Simulation of the transient recruitment of myosin (following initiation of calcium twitch) directly results in the prediction of expected patterns of ventricular pressure predicted over a cardiac cycle. To our knowledge, this investigation constitutes the first model of the myocardium that incorporates a thermodynamically motivated transient actin-myosin cross-bridge cycling framework for the simulation of myofibril contractility and remodelling. While a number of previous studies of crossbridge cycling have proposed kinetic equations to describe myosin binding (Huxley and Simmons, 1971; Offer and Ranatunga, 2013; Pate and Cooke, 1989), they consider simplified 1-D analytical solutions, e.g. twitch response of a single cross-bridge, or response to infinitesimal step stretch. Such cross-bridge formulations have not previously been incorporated into finite element heart models, and therefore their ability to uncover the link between contractility and remodelling has not been explored or established. This novel approach proposed in the current study may be readily be incorporated into existing finite element models of the heart in place of phenomenological contractility formulations (Baillargeon *et al.* 2014; Chabiniok *et al.* 2016; Pezzuto *et al.* 2014).

This study also investigates deviations from healthy homeostatic boundary conditions in order to assess the ability of the thermodynamic cross-bridge cycling framework to predict changes in structure and function under altered biomechanical conditions. Eccentric hypertrophy, whereby the number of in-series sarcomeres increases in the myocardial wall, is associated with an increased diastolic ventricular blood inflow (Yoshida et al. 2010; Costabal et al. 2019). We demonstrate the increased stretch reduces the overlap $\hat{s}$ of the actin and myosin filaments within individual sarcomeres. In order to reduce their free energy (i.e. maximise the potential sarcomere stress σ_s via increasing the availability of myosin heads), the myofibrils add additional sarcomeres $\hat{n}$ in-series to reduce individual sarcomere strain $\tilde{\varepsilon}_f$, thereby improving the overlap. Such remodelling of $\hat{n}$ is consistent with observations following the onset of eccentric hypertrophy

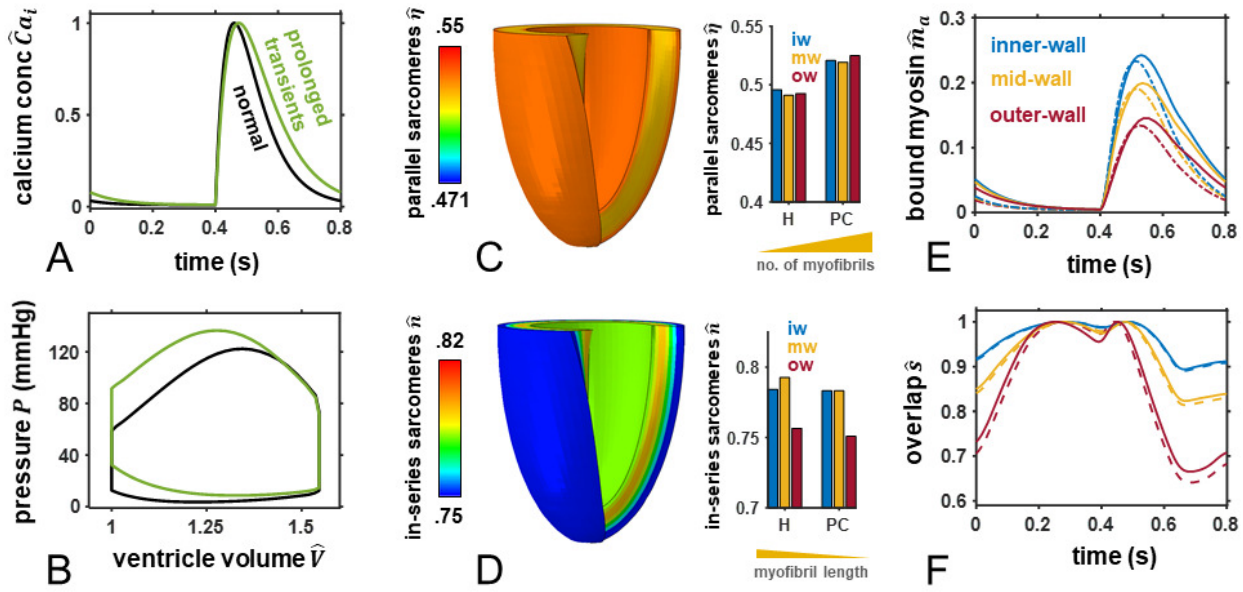

Figure 8: Prolonged calcium transients (PC): A) Calcium concentration and B) predicted pressure-volume loop over a single cardiac cycle (black line shows the healthy state for reference); Contour plots are shown at peak systole ($t = 0.552s$) for C) the concentration of myofibrils $\hat{\eta}$ and d) the number of in-series sarcomeres $\hat{n}$. Adjoining bar plots show local values in zones iw, mw, and ow with reference to healthy state; For a single cardiac cycle the predicted E) number of attached myosin heads $\hat{m}_a$ (dotted line shows healthy state for reference) and F) overlap $\hat{s}$ of the actin and myosin filaments are shown for zones iw, mw, and ow (dotted lines show the overlap $\hat{s}$ prior to remodelling of $\hat{\eta}$ and $\hat{n}$). For PC analysis $\tau_{ca} = 75\ ms$.

(Sawada and Kawamura 1991; Gerdes *et al.* 1992). Our models also predict a reduction in myofibril concentration in response to such an increased diastolic volume, resulting in a reduction of the overall contractility of the myocardium. As a result of exponential strain stiffening in the anisotropic hyperelastic formulation for the passive component of the myocardium, the changes in diastolic blood volume simulated in this study are lower than those typically measured, particularly for cases of valve regurgitation. A modification of the form of the passive hyperelastic component should be considered in a follow-on study in order to simulate higher diastolic blood volume, which will directly result in a further increase in $\hat{n}$. However, the primary aim of the current paper is to uncover the biomechanisms of active contractility and remodelling, rather than the identification of the precise hyperelastic form of the passive myocardium.

At the cell level, concentric hypertrophy is characterised by increased myofibril formation in parallel (Sawada and Kawamura 1991; Russell *et al.* 2010; Chien *et al.* 1993). In this study, we investigated the influence of (i) prolonged valve close time, (ii) prolonged calcium transients, and (iii) increased protein synthesis on myofibril remodelling. Our models suggest cross-bridge cycling (within the sarcomere/myofibril) is highly sensitive to loading conditions applied to the myocardial wall. Changes in myosin recruitment and cross-bridge cycling is a significant driving factor in myofibril remodelling, due to the free energy dependence on sarcomere stress. As an example, conditions that increase the duration of aortic valve closure maintain the sarcomere close to isometric conditions for longer, promoting increased myosin recruitment and therefore increased myofibril formation. Our results demonstrate that such increases in parallel concentration of myofibrils, associated with concentric hypertrophy, result directly from strain rate induced increases in cross-bridge formation. As suggested by Grossman *et al.* (1975), the resultant increase in ventricle blood pressure is an outcome of the mechanisms leading to such remodelling, rather than a root cause.

Increases in myofibril concentrations are predicted for prolonged calcium transients; via unblocking of actin binding sites additional myosin heads may attach. Calcium channel blockers have been shown to prevent the development of hypertrophy and are one of the main drug groups used in treatment (Gregor and Čurila, 2015). The findings in this study provide insight into the mechanisms by which such treatment is effective. Additionally, previous studies have suggested that pressure overload causes increased protein synthesis (Carabello, 2002; Cooper, 1997; Imamura et al., 1994). It is demonstrated that such synthesis is a significant driving factor in myofibril formation. With a higher density of unbound contractile proteins available, more myofibrils form in order to maintain chemical equilibrium.

Rodriguez *et al.* (1994) developed a framework for volumetric growth in a continuum mechanics setting. Through decomposition of the deformation gradient into an elastic and growth component, changes in the material volume are driven by a variable of interest (e.g. strain). In recent years with the advent of powerful computational modelling tools and facilities, this growth model has been integrated into full 3D models of the heart and used to

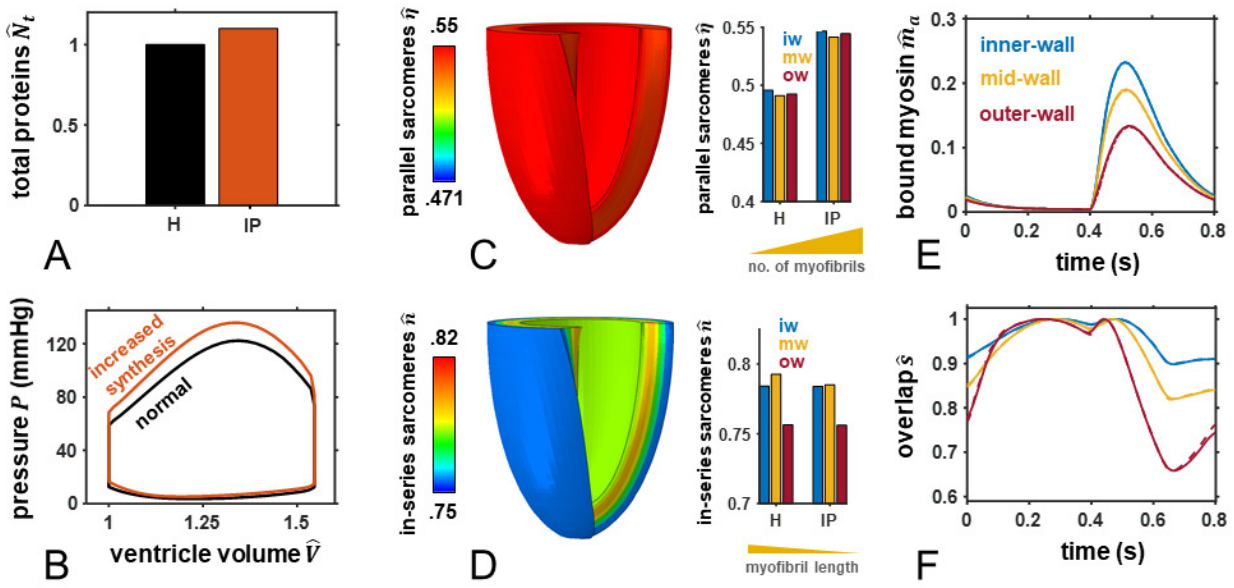

Figure 9: Increased protein synthesis (IP): A) Bar plot of total number of contractile proteins; B) Predicted pressure-volume loop over a single cardiac cycle (black line shows the healthy state for reference); Contour plots are shown at peak systole ($t = 0.552s$) for C) the concentration of myofibrils $\hat{\eta}$ and D) the number of in-series sarcomeres $\hat{n}$. Adjoining bar plots show local values in zones iw, mw, and ow with reference to healthy state; For a single cardiac cycle the predicted E) number of attached myosin heads $\hat{m}_a$ (dotted line shows healthy state for reference) and F) overlap $\hat{s}$ of the actin and myosin filaments are shown for zones iw, mw, and ow (dotted lines show the overlap $\hat{s}$ prior to remodelling of $\hat{\eta}$ and $\hat{n}$). For IP analysis $\hat{N}_t = 1.1$.

simulate cardiac hypertrophy (Rausch *et al.* 2011; Kerckhoffs *et al.* 2012), and the pathologies of diastolic and systolic heart failure (Genet et al., 2016). In such phenomeno logical models, growth is driven by changes in stress or strain from homeostatic reference values. However, the biophysical mechanisms underlying remodelling at a sub-cellular scale are typically not considered. Our thermodynamically motivated cross-bridge cycling model uncovers the link between sub-cellular processes and biomechanically induced myofibril remodelling, and could be coupled with existing growth formulations to develop a thermodynamically motivated model for tissue growth.

In this study we have demonstrated that the thermodynamics of sarcomere-level remodelling represents the first and fundamental step in tissue-/organ-level remodelling. A number of follow-on studies should be performed to explore the broad applicability of the model for clinical diagnosis. Future computational implementations will build upon our thermodynamically motivated framework to consider realistic patient geometries, fluid-structure interactions to motivate ventricle pressure and volume, cellular growth and reorientation, ECM remodelling, non-uniform calcium transients, detailed calcium/troponin/tropomyosin dynamics (Rice et al., 2003), the role of titin-associated signalling (Krüger and Kötter, 2016), and cell/tissue viscoelasticity (Reynolds et al. 2014; Reynolds and McGarry 2015). Our previous multi-scale micromechanical approach will also be extended to analyse cell interactions with the myocardium ECM, including morphological changes in cardiomyocytes and focal adhesion formation (McEvoy *et al.* 2017; McEvoy et al. 2018). Additionally, the energetic mechanisms that lead to increase protein synthesis associated with concentric hypertrophy should be investigated.

Acknowledgements. Funding support was provided by the Irish Research Council (IRC) postgraduate scholarship (GOIPG/2015/2954), the National University of Ireland Galway Hardiman scholarship, and the Science Foundation Ireland (18/ERCD/5481). The authors would like to acknowledge the Irish Centre for High-End Computing (ICHEC) for provision of computational facilities and support.

Supplementary Information

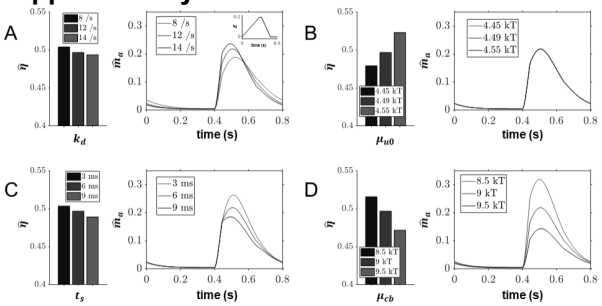

Figure S1: Influence of calibrated parameters on sarcomere remodelling: effect of A) rate coefficient k_d, B) standard enthalpy of unbound sarcomere proteins μ_{u0}, C) myosin head attachment time t_s, and D) attached/unattached myosin enthalpy difference $\Delta\mu_{cb}$ on myofibril concentration $\hat{\eta}$ and number of attached myosin heads $\hat{m}_a$ under idealised loading (see strain in inset of (A)). All other parameters and conditions are as reported for the healthy heart state.

Bibliography

Ashikaga, H., Coppola, B. a, Yamazaki, K.G., Villarreal, F.J., Omens, J.H., Covell, J.W., 2008. Changes in regional myocardial volume during the cardiac cycle: implications for transmural blood flow and cardiac structure. Am. J. Physiol. Heart Circ. Physiol. 295, H610–H618. https://doi.org/10.1152/ajpheart.00107.2008

Baillargeon, B., Rebelo, N., Fox, D.D., Taylor, R.L., 2014. The Living Heart Project: A robust and integrative simulator for human heart function. Eur. J. Mech. - A/Solids 48, 38–47. https://doi.org/10.1016/j.euromechsol.2014.04.001

Balke, C., Shorofsky, S.R., 1998. Alterations in calcium handling in cardiac hypertrophy and heart failure. Cardiovasc. Res. 37, 290–299. https://doi.org/10.1016/S0008-6363(97)00272-1

Bartoo, M.L., Linke, W.A., Pollack, G.H., 1997. Basis of passive tension and stiffness in isolated rabbit myofibrils. Am. J. Physiol. 273, C266-76. https://doi.org/10.1152/ajpcell.1997.273.1.C266

Bentivegna, L.A., Ablin, L.W., Kihara, Y., Morgan, J.P., 1991. Altered calcium handling in left ventricular pressure-overload hypertrophy as detected with aequorin in the isolated, perfused ferret heart. Circ. Res. 69, 1538–45. https://doi.org/10.1161/01.RES.69.6.1538

Bergel, D., Hunter, P., 1979. The mechanics of the heart, in: Hwang, H., Gross, D., Patel, D. (Eds.), Quantitative Cardiovascular Studies, Clinical and Research Applications of Engineering Principles. University Park Press, Baltimore, pp. 151–213.

Bootman, M.D., Bultynck, G., 2019. Fundamentals of Cellular Calcium Signaling: A Primer. Cold Spring Harb. Perspect. Biol. a038802. https://doi.org/10.1101/cshperspect.a038802

Carabello, B.A., 2013. Introduction to Aortic Stenosis. Circ. Res. 113, 179–185. https://doi.org/10.1161/CIRCRESAHA.113.300156

Carabello, B.A., 2002. Concentric versus eccentric remodeling. J. Card. Fail. 8, S258–S263. https://doi.org/10.1054/JCAF.2002.129250

Carabello, B.A., 1996. Models of volume overload hypertrophy. J. Card. Fail. 2, 55–64. https://doi.org/10.1016/S1071-9164(96)80010-8

Carabello, B.A., Paulus, W.J., 2009. Aortic stenosis. Lancet 373, 956–966. https://doi.org/10.1016/S0140-6736(09)60211-7

Chabiniok, R., Wang, V.Y., Hadjicharalambous, M., Asner, L., Lee, J., Sermesant, M., Kuhl, E., Young, A.A., Moireau, P., Nash, M.P., Chapelle, D., Nordsletten, D.A., 2016. Multiphysics and multiscale modelling, data–model fusion and integration of organ physiology in the clinic: ventricular cardiac mechanics. Interface Focus 6, 20150083. https://doi.org/10.1098/rsfs.2015.0083

Chien, K., Zhu, H., Knowlton, K., 1993. Transcriptional regulation during cardiac growth and development. Annu. Rev.

Cho, I.-J., Chang, H.-J., Park, H.-B., Heo, R., Shin, S., Shim, C.Y., Hong, G.-R., Chung, N., 2015. Aortic calcification is associated with arterial stiffening, left ventricular hypertrophy, and diastolic dysfunction in elderly male patients with hypertension. J. Hypertens. 33, 1633–1641. https://doi.org/10.1097/HJH.0000000000000607

Cooper, G., 1997. BASIC DETERMINANTS OF MYOCARDIAL HYPERTROPHY: A Review of Molecular Mechanisms. Annu. Rev. Med. 48, 13–23. https://doi.org/10.1146/annurev.med.48.1.13

de Simone, G., 2004. Concentric or Eccentric Hypertrophy: How Clinically Relevant Is the Difference? Hypertension 43, 714–715. https://doi.org/10.1161/01.HYP.0000121363.08252.a7

Dokos, S., Smaill, B.H., Young, A. a, LeGrice, I.J., 2002. Shear properties of passive ventricular myocardium. Am. J. Physiol. Heart Circ. Physiol. 283, H2650–H2659. https://doi.org/10.1152/ajpheart.00111.2002

Frampton, J.E., Orchard, C.H., Boyett, M.R., 1991. Diastolic, systolic and sarcoplasmic reticulum [Ca2+] during inotropic interventions in isolated rat myocytes. J. Physiol. 437, 351–375. https://doi.org/10.1113/jphysiol.1991.sp018600

Gaasch, W.H., Meyer, T.E., 2008. Left Ventricular Response to Mitral Regurgitation. Circulation 118, 2298–2303. https://doi.org/10.1161/CIRCULATIONAHA.107.755942

Genet, M., Lee, L.C., Baillargeon, B., Guccione, J.M., Kuhl, E., 2016. Modeling Pathologies of Diastolic and Systolic Heart Failure. Ann. Biomed. Eng. 44, 112–127. https://doi.org/10.1007/s10439-015-1351-2

Gerdes, A., Kellerman, S., Moore, J., 1992. Structural remodeling of cardiac myocytes in patients with ischemic cardiomyopathy. Circulation 86.

Göktepe, S., Acharya, S.N.S., Wong, J., Kuhl, E., 2011. Computational modeling of passive myocardium. Int. j. numer. method. biomed. eng. 27, 1–12. https://doi.org/10.1002/cnm.1402

Gotzmann, M., Lindstaedt, M., Mügge, A., 2012. From pressure overload to volume overload: Aortic regurgitation after transcatheter aortic valve implantation. Am. Heart J. 163, 903–911. https://doi.org/10.1016/j.ahj.2012.03.017

Gregor, P., Čurila, K., 2015. Medical treatment of hypertrophic cardiomyopathy – What do we know about it today? Cor Vasa 57, e219–e224. https://doi.org/10.1016/J.CRVASA.2015.02.003

Grossman, W., Jones, D., McLaurin, L.P., 1975. Wall stress and patterns of hypertrophy in the human left ventricle. J. Clin. Invest. 56, 56–64. https://doi.org/10.1172/JCI108079

Harris, S.P., Lyons, R.G., Bezold, K.L., 2011. In the thick of it: HCM-causing mutations in myosin binding proteins of the thick filament. Circ. Res. 108, 751–764. https://doi.org/10.1161/CIRCRESAHA.110.231670

Holzapfel, G.A., Ogden, R.W., 2009. Constitutive modelling of passive myocardium: a structurally based framework for material characterization. Philos. Trans. A. Math. Phys. Eng. Sci. 367, 3445–75. https://doi.org/10.1098/rsta.2009.0091

Hunter, P.J., McCulloch, A.D., ter Keurs, H.E.D.J., 1998. Modelling the mechanical properties of cardiac muscle. Prog. Biophys. Mol. Biol. 69, 289–331. https://doi.org/10.1016/S0079-6107(98)00013-3

Huxley, A.F., 1957. Muscle structure and theories of contraction. Prog. Biophys. Biophys. Chem. 7, 255–318.

Huxley, A.F., Simmons, R.M., 1971. Proposed Mechanism of Force Generation in Striated Muscle. Nature 233, 533–538. https://doi.org/10.1038/233533a0

Imamura, T., McDermott, P.J., Kent, R.L., Nagatsu, M., Cooper, G., Carabello, B.A., 1994. Acute changes in myosin heavy chain synthesis rate in pressure versus volume overload. Circ. Res. 75, 418–425. https://doi.org/10.1161/01.RES.75.3.418

Kerckhoffs, R.C.P., Omens, J., McCulloch, A.D., 2012. A single strain-based growth law predicts concentric and eccentric cardiac growth during pressure and volume overload. Mech. Res. Commun. 42, 40–50. https://doi.org/10.1016/j.mechrescom.2011.11.004

Knöll, R., Hoshijima, M., Hoffman, H.M., Person, V., Lorenzen-Schmidt, I., Bang, M.-L., Hayashi, T., Shiga, N., Yasukawa, H., Schaper, W., McKenna, W., Yokoyama, M., Schork, N.J., Omens, J.H., McCulloch, A.D., Kimura, A., Gregorio, C.C., Poller, W., Schaper, J., Schultheiss, H.P., Chien, K.R., 2002. The cardiac mechanical stretch sensor machinery involves a Z disc complex that is defective in a subset of human dilated cardiomyopathy. Cell 111, 943–55.

Krüger, M., Kötter, S., 2016. Titin, a central mediator for hypertrophic signaling, exercise-induced mechanosignaling and skeletal muscle remodeling. Front. Physiol. https://doi.org/10.3389/fphys.2016.00076

Kupari, M., Turto, H., Lommi, J., 2005. Left ventricular hypertrophy in aortic valve stenosis: preventive or promotive of systolic dysfunction and heart failure? Eur. Heart J. 26, 1790–1796. https://doi.org/10.1093/eurheartj/ehi290

Legrice, I.J., Hunter, P.J., Smaill, B.H., 1997. Laminar structure of the heart: a mathematical model. Am. J. Physiol. 272, H2466–H2476.

LeGrice, I.J., Smaill, B.H., Chai, L.Z., Edgar, S.G., Gavin, J.B., Hunter, P.J., 1995. Laminar structure of the heart: ventricular myocyte arrangement and connective tissue architecture in the dog. Am J Physiol 269, H571-82.

Linke, W.A., Popov, V.I., Pollack, G.H., 1994. Passive and active tension in single cardiac myofibrils. Biophys. J. 67, 782–92. https://doi.org/10.1016/S0006-3495(94)80538-7

Lorell, B.H., Carabello, B.A., 2000. Left ventricular hypertrophy: pathogenesis, detection, and prognosis. Circulation 102, 470–9.

Maurer, G., 2006. Aortic regurgitation. Heart 92, 994–1000. https://doi.org/10.1136/hrt.2004.042614

McEvoy, E., Deshpande, V.S., McGarry, P., 2019. Transient active force generation and stress fibre remodelling in cells under cyclic loading. Biomech. Model. Mechanobiol. 18, 921–937. https://doi.org/10.1007/s10237-019-01121-9

McEvoy, E., Deshpande, V.S., McGarry, P., 2017. Free energy analysis of cell spreading. J. Mech. Behav. Biomed. Mater. 74, 283–295. https://doi.org/10.1016/J.JMBBM.2017.06.006

Mcevoy, E., Holzapfel, G.A., Mcgarry, P., 2018. Compressibility and Anisotropy of the Ventricular Myocardium: Experimental Analysis and Microstructural Modeling. J. Biomech. Eng. https://doi.org/10.1115/1.4039947

McEvoy, E., Shishvan, S.S., Deshpande, V.S., McGarry, J.P., 2018. Thermodynamic Modeling of the Statistics of Cell Spreading on Ligand-Coated Elastic Substrates. Biophys. J. 115, 2451–2460. https://doi.org/10.1016/j.bpj.2018.11.007

Millman, B.M., 1998. The Filament Lattice of Striated Muscle. Physiol. Rev. 78, 359–391. https://doi.org/10.1152/physrev.1998.78.2.359

Nguyen, N., Nguyen, W., Nguyenton, B., Ratchada, P., Page, G., Miller, P.E., Ghetti, A., Abi-Gerges, N., 2017. Adult Human Primary Cardiomyocyte-Based Model for the Simultaneous Prediction of Drug-Induced Inotropic and Pro-arrhythmia Risk. Front. Physiol. 8, 1073. https://doi.org/10.3389/fphys.2017.01073

Nolan, D.R.., Gower, A.L., Destrade, M., Ogden, R.W., McGarry, J.P., 2014. A robust anisotropic hyperelastic formulation for the modelling of soft tissue. J. Mech.

Behav. Biomed. Mater. 39, 48–60. https://doi.org/10.1016/j.jmbbm.2014.06.016

Offer, G., Ranatunga, K.W., 2013. A Cross-Bridge Cycle with Two Tension-Generating Steps Simulates Skeletal Muscle Mechanics. Biophys. J. 105, 928–940. https://doi.org/10.1016/J.BPJ.2013.07.009

Pate, E., Cooke, R., 1989. A model of crossbridge action: the effects of ATP, ADP and Pi. J. Muscle Res. Cell Motil. 10, 181–196. https://doi.org/10.1007/BF01739809

Pezzuto, S., Ambrosi, D., Quarteroni, A., 2014. An orthotropic active-strain model for the myocardium mechanics and its numerical approximation. Eur. J. Mech. A/Solids 48, 83–96. https://doi.org/10.1016/j.euromechsol.2014.03.006

Rausch, M.K., Dam, A., Göktepe, S., Abilez, O.J., Kuhl, E., 2011. Computational modeling of growth: Systemic and pulmonary hypertension in the heart. Biomech. Model. Mechanobiol. 10, 799–811. https://doi.org/10.1007/s10237-010-0275-x

Reynolds, N.H., McGarry, J.P., 2015. Single cell active force generation under dynamic loading - Part II: Active modelling insights. Acta Biomater. 27, 251–263. https://doi.org/10.1016/j.actbio.2015.09.004

Reynolds, N.H., Ronan, W., Dowling, E.P., Owens, P., McMeeking, R.M., McGarry, J.P., 2014. On the role of the actin cytoskeleton and nucleus in the biomechanical response of spread cells. Biomaterials 35, 4015–4025. https://doi.org/10.1016/j.biomaterials.2014.01.056

Rice, J.J., Stolovitzky, G., Tu, Y., De Tombet, P.P., 2003. Ising model of cardiac thin filament activation with nearest-neighbor cooperative interactions. Biophys. J. 84, 897–909. https://doi.org/10.1016/S0006-3495(03)74907-8

Rodriguez, E.K., Hoger, A., McCulloch, A.D., 1994. Stress-dependent finite growth in soft elastic tissues. J. Biomech. 27, 455–467. https://doi.org/10.1016/0021-9290(94)90021-3

Russell, B., Curtis, M.W., Koshman, Y.E., Samarel, A.M., 2010. Mechanical stress-induced sarcomere assembly for cardiac muscle growth in length and width. J. Mol. Cell. Cardiol. 48, 817–823. https://doi.org/10.1016/J.YJMCC.2010.02.016

Sahli Costabal, F., Choy, J.S., Sack, K.L., Guccione, J.M., Kassab, G.S., Kuhl, E., 2019. Multiscale characterization of heart failure. Acta Biomater. 86, 66–76. https://doi.org/10.1016/J.ACTBIO.2018.12.053

Sawada, K., Kawamura, K., 1991. Architecture of myocardial cells in human cardiac ventricles with concentric and eccentric hypertrophy as demonstrated by quantitative scanning electron microscopy. Heart Vessels 6, 129–142. https://doi.org/10.1007/BF02058278

Sengupta, P.P., Tajik, A.J., Chandrasekaran, K., Khandheria, B.K., 2008. Twist Mechanics of the Left Ventricle. JACC Cardiovasc. Imaging 1.

Smith, D.A., Geeves, M.A., 1995. Strain-dependent cross-bridge cycle for muscle. Biophys. J. 69, 524–537. https://doi.org/10.1016/S0006-3495(95)79926-X

Sommer, G., Schriefl, A.J., Andrä, M., Sacherer, M., Viertler, C., Wolinski, H., Holzapfel, G.A., 2015. Biomechanical properties and microstructure of human ventricular myocardium. Acta Biomater. 24, 172–192. https://doi.org/10.1016/j.actbio.2015.06.031

Sommer, J.R., Johnson, E.A., 1979. Ultrastructure of cardiac muscle, in: Handbook of Physiology. The Cardiovascular System. American Physiological Society, Bethesda, MA, pp. 113–186.

Tang, Y., Nyengaard, J.R., Andersen, J.B., Baandrup, U., Gundersen, H.J.G., 2009. The Application of Stereological Methods for Estimating Structural Parameters in the Human Heart. Anat. Rec. Adv. Integr. Anat. Evol. Biol. 292, 1630–1647. https://doi.org/10.1002/ar.20952

Vigliotti, A., Ronan, W., Baaijens, F.P.T., Deshpande, V.S., 2015. A thermodynamically motivated model for stress-fiber reorganization. Biomech. Model. Mechanobiol. https://doi.org/10.1007/s10237-015-0722-9

Wang, V.Y., Hoogendoorn, C., Frangi, A.F., Cowan, B.R., Hunter, P.J., Young, A.A., Nash, M.P., 2013. LNCS 7746 - Automated Personalised Human Left Ventricular FE Models to Investigate Heart Failure Mechanics. LNCS 7746, 307–316.

Yeoh, O.H., 1993. Some Forms of the Strain Energy Function for Rubber. Rubber Chem. Technol. 66, 754–771. https://doi.org/10.5254/1.3538343

Yoshida, M., Sho, E., Nanjo, H., Takahashi, M., Kobayashi, M., Kawamura, K., Honma, M., Komatsu, M., Sugita, A., Yamauchi, M., Hosoi, T., Ito, Y., Masuda, H., 2010. Weaving Hypothesis of Cardiomyocyte Sarcomeres: Discovery of Periodic Broadening and Narrowing of Intercalated Disk during Volume-Load Change. Am. J. Pathol. 176, 660–678. https://doi.org/10.2353/AJPATH.2010.090348

Zhou, P., Pu, W.T., 2016. Recounting Cardiac Cellular Composition. Circ. Res. 118, 368–70. https://doi.org/10.1161/CIRCRESAHA.116.308139